Impact of tumor-specific targeting on the biodistribution and efficacy of siRNA nanoparticles measured by multimodality *in vivo* imaging

Derek W. Bartlett*, Helen Su†, Isabel J. Hildebrandt†, Wolfgang A. Weber†‡, and Mark E. Davis*§

*Chemical Engineering, California Institute of Technology, 1200 East California Boulevard, MC 210-41, Pasadena, CA 91125; †Department of Molecular and Medical Pharmacology, David Geffen School of Medicine, University of California, 650 Charles Young Drive, CHS AR-274, Los Angeles, CA 90095; and ‡Division of Nuclear Medicine, University of Freiburg, Hugstetterstrasse 55, 79106 Freiburg, Germany

Contributed by Mark E. Davis, August 7, 2007 (sent for review July 5, 2007)

Targeted delivery represents a promising approach for the development of safer and more effective therapeutics for oncology applications. Although macromolecules accumulate nonspecifically in tumors through the enhanced permeability and retention (EPR) effect, previous studies using nanoparticles to deliver chemotherapeutics or siRNA demonstrated that attachment of cell-specific targeting ligands to the surface of nanoparticles leads to enhanced potency relative to nontargeted formulations. Here, we use positron emission tomography (PET) and bioluminescent imaging to quantify the *in vivo* biodistribution and function of nanoparticles formed with cyclodextrin-containing polycations and siRNA. Conjugation of 1,4,7,10-tetraazacyclododecane-1,4,7,10-tetraacetic acid to the 5′ end of the siRNA molecules allows labeling with ^{64}Cu for PET imaging. Bioluminescent imaging of mice bearing luciferase-expressing Neuro2A s.c. tumors before and after PET imaging enables correlation of functional efficacy with biodistribution data. Although both nontargeted and transferrin-targeted siRNA nanoparticles exhibit similar biodistribution and tumor localization by PET, transferrin-targeted siRNA nanoparticles reduce tumor luciferase activity by ≈50% relative to nontargeted siRNA nanoparticles 1 d after injection. Compartmental modeling is used to show that the primary advantage of targeted nanoparticles is associated with processes involved in cellular uptake in tumor cells rather than overall tumor localization. Optimization of internalization may therefore be key for the development of effective nanoparticle-based targeted therapeutics.

kinetic modeling | multimodality imaging | targeted delivery | tumor uptake

Targeted nanoparticles are a promising class of new experimental medicines that have the potential to provide increased efficacy and lower toxicity relative to conventional therapeutics. Through the enhanced permeability and retention (EPR) effect, macromolecular therapeutics tend to accumulate within tumors after systemic delivery (1). As such, nanoparticles represent an approach for the delivery of large drug payloads to tumors. However, because many drugs require cellular internalization for efficacy, accumulation within the tumor microenvironment by the EPR effect may not correlate with therapeutic outcome.

siRNA molecules are short double-stranded nucleic acid molecules that can act as mediators of RNAi within the cytoplasm of a cell. Therapeutic application of siRNAs requires their effective delivery into the target cells of interest, because naked siRNAs do not enter most cell types on their own. To address the challenge of nucleic acid delivery, a variety of methodologies have been developed with varying success, including covalent attachment of cholesterol, interaction with antibody-protamine fusion proteins, liposome encapsulation, or nanoparticle formation with cationic lipids or polymers (2–6).

Targeted delivery approaches involve the use of cell-specific targeting ligands that can bind to surface receptors on cells. Recent reports have highlighted the importance of these targeting ligands for efficacy when delivering a variety of payloads (7–10). For example, anti-HER2 immunoliposomes containing doxorubicin achieved greater antitumor efficacy relative to nontargeted liposomes in HER2-overexpressing human breast cancer xenografts, but this difference in antitumor efficacy was not observed in non-HER2-overexpressing tumor xenografts (9). Additionally, transferrin (Tf)-targeted nanoparticles formed by using cyclodextrin-containing polycations and siRNA led to significant inhibition of tumor growth in a disseminated model of Ewing's sarcoma, whereas an identical nanoparticle formulation without Tf did not lead to such tumor growth inhibition (10). This result is consistent with two previous reports using this system to deliver plasmid DNA[¶] and a DNAzyme (11) that showed that the amount of nucleic acid reaching tumors did not depend on the presence of Tf, but plasmid expression[¶] and intracellular localization within tumor cells (11) occurred only with the Tf-targeted nanoparticles.

Although targeted nanoparticles appear to display enhanced potency relative to nontargeted nanoparticles, this is not necessarily a result of increased tumor uptake. Kirpotin *et al.* (12) established that attachment of antibody targeting ligands to long-circulating nanoparticles increases cellular internalization without affecting overall tumor uptake. This behavior may be unexpected because the targeting ligands alone do show enhanced uptake within tumors expressing the relevant antigen (13). Relatively few studies have attempted to address how the pharmacokinetics and biodistribution of nanoparticles are affected by attachment of targeting ligands, yet such studies will be critical for designing more effective nanoparticle carriers. Medarova *et al.* (14) described the use of MRI and fluorescence imaging to monitor the local tumor accumulation and functional activity of magnetic nanoparticles covalently linked to siRNAs. That study illustrated the power of using multimodality imaging approaches to correlate localization of therapeutic entities to their biological activity.

Here, we employ positron emission tomography (PET)/computer tomography (CT) to monitor whole-body biodistribution kinetics and tumor localization of siRNA nanoparticles while

Author contributions: D.W.B., H.S., W.A.W., and M.E.D. designed research; D.W.B., H.S., and I.J.H. performed research; D.W.B., H.S., W.A.W., and M.E.D. analyzed data; and D.W.B. wrote the paper.

Conflict of interest statement: M.E.D. is a consultant to and has stock in Calando Pharmaceuticals.

Freely available online through the PNAS open access option.

Abbreviations: BLI, bioluminescent imaging; CT, computer tomography; DOTA, 1,4,7,10-tetraazacyclododecane-1,4,7,10-tetraacetic acid; EPR, enhanced permeability and retention; ID, injected dose; PET, positron emission tomography; Tf, transferrin.

§To whom correspondence should be addressed. E-mail: mdavis@cheme.caltech.edu.

[¶]Bellocq, N. C., Davis, M. E., Engler, H., Jensen, G. S., Liu, A., Machemer, T., Maneval, D. C., Quijano, E., Pun, S. H., Schluep, T., Wen, S. (2003) *Mol Ther* 7:S290 (abstr.).

This article contains supporting information online at www.pnas.org/cgi/content/full/0707461104/DC1.

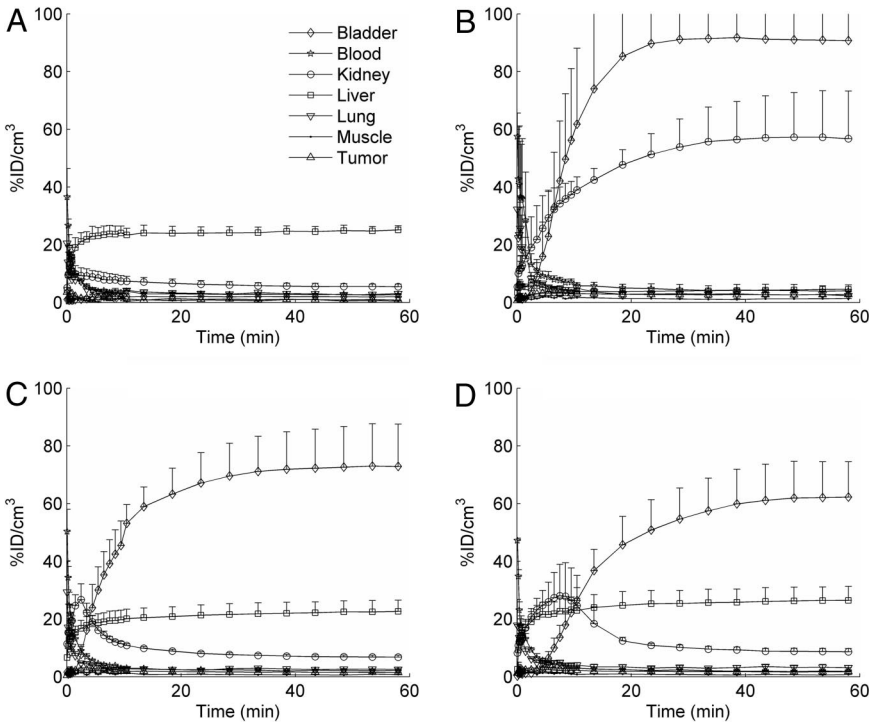

Fig. 1. Average time–activity curves for the first 60 min after injection. Data are shown for mice injected with ^{64}Cu (*A*), ^{64}Cu-labeled DOTA (*B*), ^{64}Cu-labeled DOTA-siRNA (*C*), and Tf-targeted nanoparticles containing ^{64}Cu-labeled DOTA-siRNA (*D*). Error bars indicate SE.

concurrently using bioluminescent imaging (BLI) to measure luciferase knockdown by the delivered siRNA molecules. By formulating nanoparticles with or without Tf targeting ligands, the effect of cell-specific targeting on both biodistribution and function can be studied simultaneously within the same animal. A mathematical model of targeted nanoparticle behavior is presented that can describe the results obtained here and illustrate concepts that can be applied generally to the design of targeted therapeutics for oncology applications.

Results

Formation of ^{64}Cu-Labeled Nanoparticles, Using 1,4,7,10-Tetraazacyclododecane-1,4,7,10-Tetraacetic Acid (DOTA)-siRNA. DOTA was conjugated to the 5′ end of an siRNA sequence targeting luciferase mRNA. A nonradioactive assay, using gadolinium, demonstrated that the DOTA-siRNA was able to bind gadolinium, and this binding efficiency was ≈50% of that observed for free DOTA. The DOTA-siRNA retained its functional capacity to silence luciferase expression, albeit at a slightly reduced potency relative to unmodified siRNA [supporting information (SI) Fig. 5]. Furthermore, the duration of luciferase knockdown is consistent with an RNAi-based mechanism (15, 16). Nanoparticles were successfully formed with DOTA-siRNA, and the fraction of the total siRNA that was modified with DOTA had a negligible effect on nanoparticle zeta potential and only a minor effect on nanoparticle size (SI Fig. 6). Nanoparticles formed with either unmodified siRNA or with DOTA-siRNA representing 20% or 50% of the total siRNA demonstrated equivalent stability against nuclease degradation of the encapsulated siRNA after incubation in mouse serum with an estimated half-life of ≈11 h (SI Fig. 7).

Biodistribution of Naked siRNA and siRNA Nanoparticles After i.v. Administration. Micro-PET/CT was used to examine the kinetics of the biodistribution and tumor localization of ^{64}Cu-labeled molecules after i.v. injection in mice. Reconstructed micro-PET/CT images of mice at 1, 10, and 60 min after injection are shown in SI Fig. 8. Images were quantified by using AMIDE software, and the percentage of injected dose (ID)/cm^3 was calculated for each region of interest over all time frames (17). The resulting time–activity curves shown in Fig. 1 represent the averages from two (^{64}Cu, ^{64}Cu-DOTA) or three (^{64}Cu-DOTA-siRNA, Tf-targeted nanoparticles) independent experiments. SI Fig. 9 contains these same time–activity curves plotted with different scales.

^{64}Cu alone accumulated rapidly in the liver, plateauing at ≈25% ID/cm^3 after only 10 min, likely resulting from binding to serum proteins (18). However, when the ^{64}Cu was chelated by DOTA and injected systemically in mice, it accumulated in the kidneys (≈57% ID/cm^3 at 60 min) and bladder (≈91% ID/cm^3 at 60 min) with very little in the liver (<5% ID/cm^3 at 60 min), consistent with the kidney clearance of other metal chelators, such as diethylenetriaminepentaacetic acid (19). When the DOTA was conjugated to an siRNA molecule and labeled with ^{64}Cu (^{64}Cu-DOTA-siRNA), the observed biodistribution kinetics were characterized by rapid blood clearance through liver accumulation (≈23% ID/cm^3 at 60 min) and kidney filtration into the bladder (≈73% ID/cm^3 at 60 min). The total siRNA administered per mouse was 2.5 mg/kg, and ≈50% of this siRNA was ^{64}Cu-DOTA-siRNA (purified by ethanol precipitation). A biexponential fit of the ^{64}Cu-DOTA-siRNA plasma concentration yielded an initial elimination half-life of 2.4 min and a terminal elimination half-life of 61.9 min. The rapid initial elimination half-life is expected for siRNA molecules whose small size (≈13 kDa) allows first-pass renal clearance, and these results, using micro-PET, are consistent with values reported in refs. 2, 20, and 21.

Micro-PET/CT was also used to examine the kinetics of the biodistribution and tumor localization of siRNA nanoparticles after i.v. injection in mice. The total dose of siRNA within the nanoparticles was the same as that used for naked siRNA (2.5 mg/kg), and again ≈50% of the total siRNA was DOTA-siRNA. The biodistribution of the ^{64}Cu-DOTA-siRNA packaged into Tf-targeted nanoparticles appeared similar to that observed for naked ^{64}Cu-

DOTA-siRNA, except that there was slightly higher liver accumulation (≈26% ID/cm^3 at 60 min) and a delayed peak in kidney accumulation (≈10 min after injection). Although liver uptake is often observed for nanoparticles because of interactions with the reticuloendothelial system, the lack of significant lung-associated activity suggests that PEGylation and Tf targeting may shield the positively charged nanoparticles and reduce nonspecific interactions (7, 8, 11, 22). These observations are also consistent with those reported by de Wolf *et al.* (23), who noted that formulation of the siRNA into polycationic carriers had little effect on the pharmacokinetics and initial tumor localization compared with naked siRNA; both naked siRNA and siRNA packaged into the carriers exhibited rapid blood clearance with tissue distribution mainly to the kidneys and liver within the first 15 min after injection.

The significant portion of the activity after injection of Tf-targeted nanoparticles that cleared rapidly through the kidneys and was excreted in the urine suggests that free siRNA may have been present, because intact nanoparticles are too large for kidney filtration into the urine. However, the nanoparticle formulations showed <10% free siRNA when analyzed by gel electrophoresis immediately before injection (SI Fig. 10). Therefore, it is possible that nanoparticle disruption and release of free siRNA after injection into the bloodstream may contribute to the similar pharmacokinetics observed for naked siRNA and siRNA nanoparticles. Because the nanoparticles are formed through electrostatic interactions, competition from electrolytes, polyanions, or polycations present within the bloodstream may destabilize the nanoparticles. No free siRNA was detected by gel electrophoresis after exposure of targeted nanoparticles to fresh mouse blood for 5 min (SI Fig. 11). However, contact of siRNA nanoparticles to increasing concentrations of NaCl did release free siRNA, with ≈50% dissociation at 0.4 M NaCl (SI Fig. 12). *SI Text* contains one hypothesis for a physiologically based mechanism that could contribute to the NaCl-mediated disruption of the nanoparticles within the kidneys. However, because the imaging methodology used here does not differentiate between intact/degraded forms of the nanoparticles or siRNA molecules, it remains unknown as to exactly how and in what form the ^{64}Cu gets into the urine (SI Fig. 13).

Tumor Localization and Function of Targeted Versus Nontargeted siRNA Nanoparticles. A multimodality imaging approach was used to investigate the biodistribution and functional activity of siRNA delivered by Tf-targeted or nontargeted nanoparticles. Micro-PET/CT permitted analysis of the biodistribution and tumor localization of the siRNA nanoparticles, whereas BLI enabled quantification of the resulting luciferase knockdown by siRNA.

Initial studies, using micro-PET/CT, revealed that the tissue distribution of the ^{64}Cu-DOTA-siRNA delivered by Tf-targeted and nontargeted nanoparticles was very similar for the first hour after injection, with similar blood clearance and tumor accumulation (Fig. 2). The combination of micro-PET/CT and BLI provided additional insights into the effect of the Tf targeting ligands, and Fig. 3 contains the micro-PET/CT images (1 d after injection) and corresponding bioluminescent images (before injection and 1 d after injection) of two representative mice. The average tumor activities at 1 d after injection measured by micro-PET were 1.1 ± 0.3% ID/cm^3 and 1.4 ± 0.4% ID/cm^3 for Tf-targeted and nontargeted nanoparticles, respectively. These same mice were also examined for luciferase activity by BLI before injection and 1 d after injection. The relative increase in tumor luciferase activity in mice treated with Tf-targeted nanoparticles was 50% lower than that in mice treated with nontargeted nanoparticles (Fig. 3*C*). These data provide strong evidence suggesting that Tf-targeted nanoparticles were able to deliver more functional siRNA into the tumor cells than nontargeted nanoparticles, even though both accumulated to a similar extent within the tumor microenvironment.

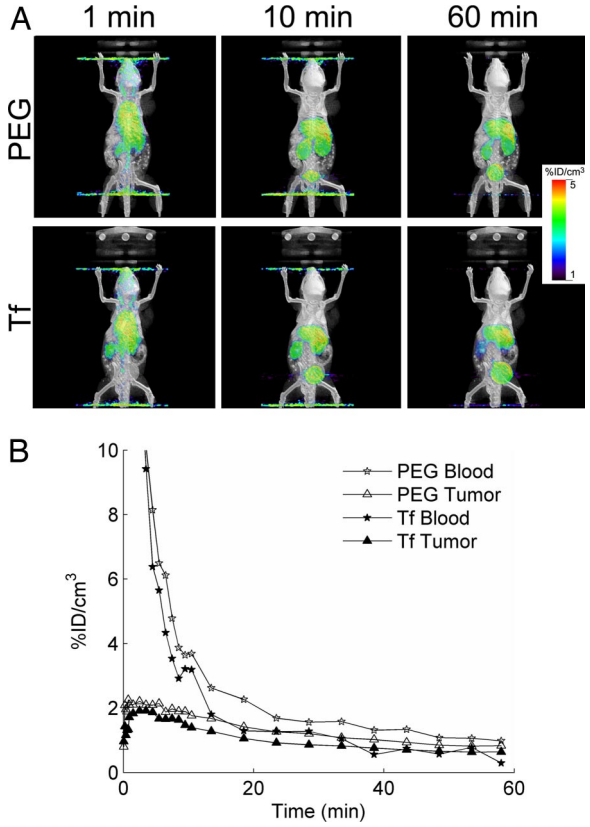

Fig. 2. Tissue distribution of ^{64}Cu-DOTA-siRNA delivered by targeted (Tf) and nontargeted (PEG) nanoparticles. (*A*) Fused micro-PET/CT images of mice at 1, 10, and 60 min after injection. (*B*) Blood clearance and tumor localization of Tf-targeted and nontargeted siRNA nanoparticles.

Compartmental Model Analysis of Tumor Localization and Uptake. Compartmental modeling provides insights into the impact that tumor-specific targeting can have on the tumor localization of systemically applied therapeutics (Fig. 4). The first term in the equation for tumor uptake ("*Total*" in Fig. 4*A*) represents the contribution from the tumor vascular space during the wash-in phase, and a rate constant of 25 min^{-1} is used to estimate the early peak after injection. A reasonable fit for targeted nanoparticle tumor uptake can be achieved if $k_{21} = 0$. Under these conditions, a two-compartment model with $k_{23} = 0$ yields the same curve for *Total* as a three-compartment model with a nonzero value for k_{23} (Fig. 4*B*). Targeting ligands that can enhance tumor-specific binding (k_{23}) are not expected to increase overall tumor uptake ($C_2 + C_3$) for entities that remain trapped in the tumor microenvironment and do not reversibly return to the blood circulation. However, simulations also show that for entities that can rapidly exchange between the blood compartment and the tumor interstitial space, tumor-specific targeting can significantly improve tumor uptake. These generalizable trends are illustrated in Fig. 4*C*. Consistent with these simulations, Adams *et al.* (24) demonstrated that an scFv (M_r 25,000) against HER2/*neu* exhibited 7-fold greater tumor accumulation than an anti-HER2/*neu* scFv with a 320-fold lower affinity. Conceptually, tumor-specific binding reduces the amount of free material that would otherwise be available for exchange with the blood compartment. This decrease in C_2 has the same consequence of enhanced tumor accumulation as a decrease in k_{21} caused by the EPR effect when the tumor uptake is measured as the total amount present (intracellular + extracellular) in the tumor microenvironment, as is done with micro-PET.

Discussion

This study demonstrates the utility of noninvasive imaging technologies to concurrently investigate the impact of cell-specific

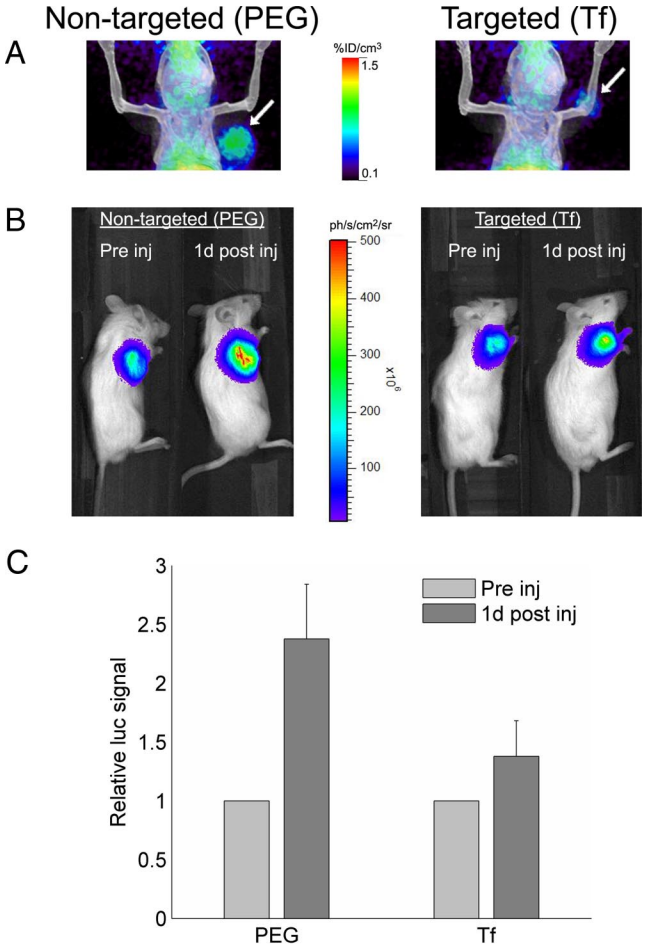

Fig. 3. Multimodality *in vivo* imaging of siRNA nanoparticle delivery and function, using micro-PET/CT and BLI. (*A*) Fused micro-PET/CT images showing tumor-associated (arrow) activity 1 d after injection of targeted (Tf) and nontargeted (PEG) nanoparticles containing ^{64}Cu-DOTA-siRNA. (*B*) BLI of the same mice shown in *A* before injection and 1 d after injection. (*C*) Relative change in luciferase expression 1 d after injection of Tf-targeted (Tf, $n = 7$) and nontargeted (PEG, $n = 4$) nanoparticles containing ^{64}Cu-DOTA-siRNA for simultaneous PET imaging. Error bars indicate SE.

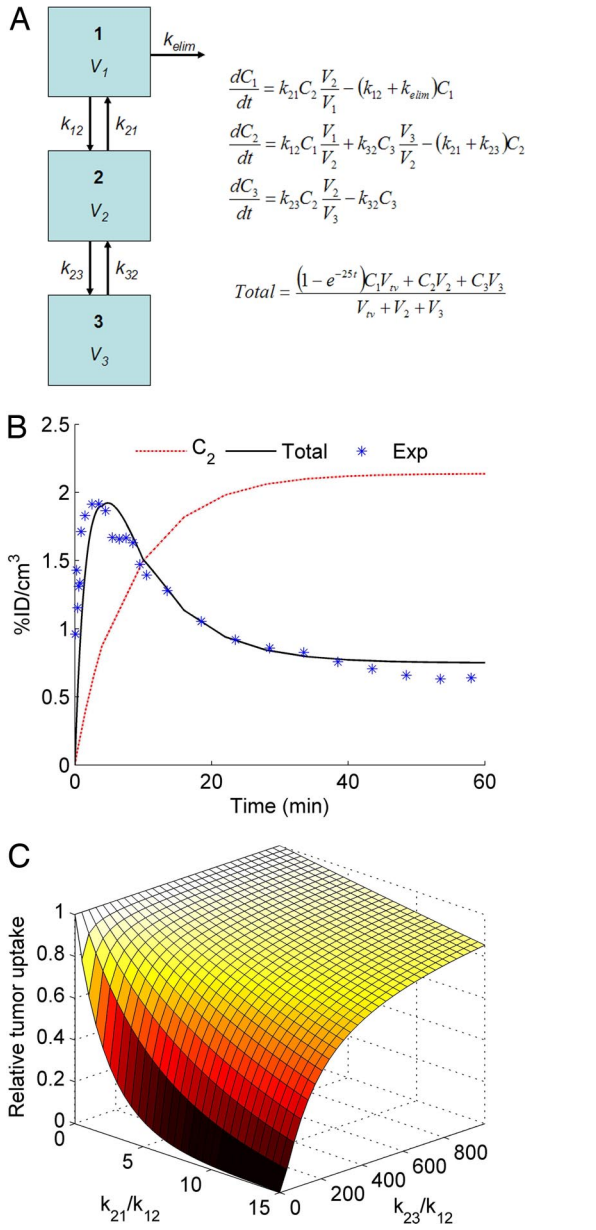

Fig. 4. Analysis of the interplay between the EPR effect and tumor-specific targeting, using a three-compartment model. (*A*) Model schematic and governing equations to estimate tumor uptake. (*B*) Model fit for total tumor uptake (Total) from experimental data (Exp) in Fig. 2, using $k_{21} = k_{23} = 0$. C_2 is the concentration in compartment 2. (*C*) Effect of tumor clearance (k_{21}) and tumor-specific binding/uptake (k_{23}) on tumor accumulation 1 d after injection.

targeting ligands on the biodistribution and function of targeted siRNA nanoparticles *in vivo*. Synthesis of DOTA-conjugated siRNA molecules enables labeling with ^{64}Cu and subsequent imaging by micro-PET, which provides high-resolution, three-dimensional biodistribution data of the injected radiolabeled molecules over time. The spatiotemporal distribution of the injected ^{64}Cu-labeled molecules was determined by coregistration of the micro-PET images with anatomical information from micro-CT. Furthermore, BLI was used to measure the relative change in luciferase activity resulting from siRNA function within the tumor cells. This methodology enables investigation of the differences in biodistribution and functional efficacy between targeted and nontargeted siRNA nanoparticles.

Attachment of the Tf targeting ligand to the surface of the nanoparticles has a negligible impact on the biodistribution observed by micro-PET. Both targeted and nontargeted nanoparticles demonstrate nearly identical tumor localization kinetics and at 1 d after injection show similar tumor accumulation (≈1% ID/cm^3). This is likely a consequence of the EPR effect, which traps macromolecules in the tumor microenvironment. Using the same delivery system carrying plasmid DNA or a DNAzyme, tumor accumulation is shown to be mouse-model-dependent and can reach ≈10% ID. Although the accumulated amounts vary with tumor type, they are not correlated to the Tf receptor status of the tumor cells (11).

BLI was used to examine function in tandem with the tissue distribution studies by micro-PET. Unlike the micro-PET results showing that the tissue distribution is approximately equal for both targeted and nontargeted nanoparticles, BLI reveals that targeted nanoparticles more effectively reduce tumor luciferase expression 1 d after injection. These results likely indicate that a higher fraction of the siRNA achieves intracellular localization and thereby functional activity within the tumor cells when delivered by using Tf-targeted nanoparticles. Previous studies with other targeted delivery systems have also suggested that the targeting moieties do not necessarily increase the total tumor accumulation but instead contribute to enhanced internalization by the tumor cells (9, 12, 25).

Table 1. Model variables

Name	Compartment	Description (units)
C_1	1, plasma	Plasma concentration (mol L^{-1})
C_2	2, interstitial (tumor)	Interstitial concentration (mol L^{-1})
C_3	3, cell-associated or intracellular (tumor)	Tumor cell-associated concentration (mol L^{-1})

This study therefore highlights the potentially important difference in the relative distribution between intracellular and extracellular tumor space for targeted and nontargeted entities. Nonspecific tumor accumulation (e.g., the EPR effect) can dominate for sufficiently large macromolecular entities, such as nanoparticles, whereas specific interaction between targeting ligands and tumor cells can drive tumor accumulation for relatively small molecules. Moreover, the physicochemical properties of nanoparticle carriers will largely determine their pharmacokinetics/biodistribution, but the presence of targeting ligands can greatly enhance intracellular uptake. Such considerations will be important for the design of molecular conjugates for imaging and therapeutic applications in oncology.

Materials and Methods

siRNA Sequence. RNA oligonucleotides were ordered from Integrated DNA Technologies (Coralville, IA). For the siRNA duplex against luciferase, the antisense strand (5′-UAUCGAAGGACUCUGGCACdTdT-3′) was ordered unmodified, whereas the sense strand (5′-GUGCCAGAGUCCUUCGAUAdTdT-3′) was ordered unmodified or with a 5′ amino modifier C6 modification on the 5′ end of the sense strand. A nontargeting control siRNA duplex was created by using unmodified versions of both the antisense (5′-UAGCGACUAAACACAUCAAUU-3′) and sense (5′-UUGAUGUGUUUAGUCGCUAUU-3′) strands.

Synthesis of DOTA-siRNA. 1,4,7,10-tetraazacyclododecane-1,4,7,10-tetraacetic acid mono(*N*-hydroxysuccinimide ester) (DOTA-NHS-ester) was ordered from Macrocyclics (Dallas, TX). The amine-modified RNA sense strand with a 100-fold molar excess of DOTA-NHS-ester in carbonate buffer (pH 9) was added to a microcentrifuge tube. The contents were reacted by stirring for ≈4 h at room temperature. The DOTA-RNAsense conjugate was ethanol-precipitated, resuspended in water, and annealed to the unmodified antisense strand to yield DOTA-siRNA. All liquids were pretreated with Chelex-100 (Bio-Rad, Hercules, CA) to remove trace metal contaminants.

Verification of DOTA-siRNA Conjugation. Equimolar amounts of gadolinium chloride ($GdCl_3$) and either DOTA or DOTA-siRNA in 0.1 M ammonium acetate buffer (pH 6) were added to a microcentrifuge tube. The microcentrifuge tubes were incubated for 15 min at 75°C for the labeling reaction. Half of the labeling reaction was combined with an equal volume of 1 mM arsenazo III, and the absorbance at 660 nm was measured by using a Safire plate reader (Tecan, Durham, NC). The presence of free gadolinium ions results in a bathochromic shift from 548 nm to 660 nm, and comparison with a standard curve allowed estimation of the amount of free gadolinium remaining.

***In Vitro* Transfection.** Neuro2A-Luc cells with constitutive luciferase expression were transfected with siRNA by using Oligofectamine (Invitrogen, Carlsbad, CA), and the kinetics of the luciferase knockdown by unmodified and DOTA-conjugated siRNA were determined by using the Xenogen (Alameda, CA) IVIS 100 as described in refs. 15 and 16.

^{64}Cu Labeling. ^{64}Cu chloride was produced at Washington University (St. Louis, MO). The ^{64}Cu chloride was mixed with citrate buffer (pH 5, 0.1 M), and DOTA or DOTA-siRNA was added to achieve a final DOTA:^{64}Cu ratio of 250:1. The mixture was incubated for 1 h at 60°C, and the DOTA-siRNA labeling reaction was purified by gel filtration or ethanol precipitation. Gel filtration was performed by using MicroSpin G-25 columns (Amersham Biosciences, Little Chalfont, U.K.) according to manufacturer's instructions. Ethanol precipitation was accomplished by adding 0.1 vol of 3 M sodium acetate and 2.5 vol of prechilled ethanol followed by incubation for ≈2 h at −80°C. The precipitated DOTA-siRNA was centrifuged, washed with 70% ethanol, and resuspended in water to yield ^{64}Cu-DOTA-siRNA.

Nanoparticle Formation. Tf-targeted and nontargeted siRNA nanoparticles were formed by using cyclodextrin-containing polycations as described in ref. 6. Typically, nanoparticles were formed in water at a charge ratio of 3 (+/−) and an siRNA concentration of 0.5 g/liter. One percent of the adamantane-PEG molecules on the surface of the targeted nanoparticles were modified with Tf (adamantane-PEG-Tf). The nanoparticles were suspended in a 5% (wt/vol) glucose carrier solution for injection.

Dynamic Light Scattering. Nanoparticles were formed in water at a charge ratio of 3 (+/−) and an siRNA concentration of 0.1 g/liter. A ZetaPALS instrument (Brookhaven Instruments, Holtsville, NY) was used to measure both the effective hydrodynamic diameter and zeta potential.

Serum Stability of siRNA Nanoparticles. Tf-targeted nanoparticles were incubated in 50% mouse serum (Sigma, St. Louis, MO) for 4 h at 37°C and 5% CO_2. Aliquots were removed at specified time points and run on an agarose gel to determine the amount of intact

Table 2. Model parameters

Name	Description (units)	Determination	Value
k_{12}	Extravasation (min^{-1})	Fit to data	3.1×10^{-4}
k_{21}	Return to blood (min^{-1})		Varied
k_{23}	Binding to or uptake by tumor cells (min^{-1})		Varied
k_{32}	Release from binding (min^{-1})	Estimated from ref. 27, mAb/TfR	7×10^{-3}
k_{elim}	Rate of elimination from blood (min^{-1})	Estimated from data in Fig. 2	0.14
V_1	Plasma volume, mouse (L)	Estimated from ref. 28	1.5×10^{-3}
V_2	Tumor interstitial volume (L)	Estimated from ref. 29, 300 mm^3 tumor	1.1×10^{-4}
V_3	Tumor cellular volume (L)	Estimated from ref. 29, 300 mm^3 tumor	1.8×10^{-4}
V_{tv}	Tumor vascular volume (L)	Estimated from ref. 29, 300 mm^3 tumor	1.5×10^{-5}

siRNA remaining. Nanoparticles incubated in water instead of mouse serum served as controls. Dissociation of the nanoparticles was achieved by adding 1% SDS immediately before gel loading. siRNA bands were visualized by ethidium bromide staining and quantified by using ImageJ software.

Salt Stability of siRNA and pDNA Nanoparticles. Tf-targeted nanoparticles were formed in water at a charge ratio of 3 (+/−) and an siRNA or pDNA concentration of 0.5 g/liter. A portion of the nanoparticle formulation (containing 1 μg of siRNA or pDNA) was added to a microcentrifuge tube and mixed with 1% SDS or NaCl at a range of concentrations from 0 to 1.5 M NaCl. The samples were allowed to incubate for 3–5 min at room temperature before being loaded into a 1% agarose gel. Bands were visualized by ethidium bromide staining, and quantification of intact siRNA or pDNA nanoparticles (bands remaining in the well at the top of the gel) was performed by using ImageJ software.

Animals and Tumor Formation. Severe combined immunodeficient (NOD/SCID) mice were purchased from The Jackson Laboratory (Bar Harbor, ME). All animal manipulations were performed with sterile technique and were approved by the University of California at Los Angeles Animal Research Committee. Neuro2A-Luc cells were cultured in DMEM supplemented with 10% FBS, 2 mg/ml glucose, 100 units/ml penicillin, and 100 units/ml streptomycin. Exponentially growing Neuro2A-Luc cells were removed from the plate with trypsin, resuspended in PBS and Matrigel (BD Biosciences, San Jose, CA), and injected s.c. into the right flank of NOD/SCID mice at 1–2 $\times$ 10^6 cells per mouse. Tumors were allowed to grow to ≈6–7 mm in diameter before injection and imaging.

Micro-PET/CT Imaging. Micro-PET/CT imaging was performed with a micro-PET FOCUS 220 PET scanner (Siemens, Malvern, PA) and a MicroCAT II CT scanner (Siemens) (23). Fifteen minutes before imaging, mice were anesthetized by using 1.5–2% isoflurane in a heated (30°C) induction chamber, then transferred to a heated isolation/imaging chamber. ^{64}Cu (100–300 μCi) (1 Ci = 37 GBq) was injected via tail vein while the anesthetized animals were positioned on the scanner bed, and a dynamic PET scan was acquired for 1 h. Mice were moved to the micro-CT in the same isolation/imaging chamber (26). PET images were reconstructed by filtered back projection, using a ramp filter to yield an image resolution of 1.7 mm. Immediately after the micro-PET scan, mice underwent a 7-min micro-CT scan, using routine image acquisition parameters (26). The micro-CT scan was used for anatomical localization of the tissue concentrations of the ^{64}Cu over time by micro-PET. Static micro-PET scans were acquired on the following day (≈18–24 h after injection) with another micro-CT scan for anatomical coregistration.

To determine temporal changes of tracer concentration in various tissues, ellipsoid regions of interest were placed in the region that exhibited the highest ^{64}Cu activity as determined by visual inspection. To ensure accurate anatomical positioning, regions of interest were placed on fused micro-PET/CT images generated by the AMIDE software (17). To minimize partial volume effects, care was taken not to include the anatomical borders of the organs. Considering the size of the studied organs and tumors and the spatial resolution of the PET scanner, partial volume effects are not expected to have a major impact on the results of quantitative analysis. Activity concentrations are expressed as percent of the decay-corrected injected activity per cm^3 of tissue (can be approximated as percentage ID/g), using the AMIDE software, and these values are normalized to an elliptic cylinder region of interest drawn over the entire mouse. Blood activities represent the whole blood volume, so plasma concentrations are ≈2-fold greater, assuming ≈50% hematocrit.

BLI. BLI was performed by using a Xenogen IVIS 100 imaging system. Mice were anesthetized with 2.5% isoflurane and injected i.p. with 0.2 ml of a 15 g/liter D-luciferin solution in PBS. Light emission was measured 10 min after injection of the D-luciferin solution, and bioluminescent signals were quantified by using Living Image software (Xenogen).

Compartmental Modeling. A three-compartment model was used to investigate the impact of tumor-specific targeting on tumor accumulation. Model variables and parameters are defined in Tables 1 and 2. The system of first-order ODEs was solved by using MATLAB (Mathworks, Natick, MA).

We thank Dr. Waldemar Ladno, Dr. David Stout, Judy Edwards, Antonia Luu, and Amanda Armijo for assistance with micro-PET/CT imaging and Calando Pharmaceuticals (Pasadena, CA) for the gift of cyclodextrin-containing polycations, adamantane-PEG, and adamantane-PEG-Tf. This work was supported by a National Science Foundation Graduate Research Fellowship (to D.W.B.) and National Cancer Institute Grant CA119347.

1. Matsumura Y, Oda T, Maeda H (1987) *Gan To Kagaku Ryoho* 14:821–829.
2. Soutschek J, Akinc A, Bramiage B, Charisse K, Constien R, Donoghue M, Elbashir S, Geick A, Hadwiger P, Harborth J, *et al.* (2004) *Nature* 432:173–178.
3. Song E, Zhu P, Lee S-K, Chowdhury D, Kussman S, Dykxhoorn DM, Feng Y, Palliser D, Weiner DB, Shankar P, *et al.* (2005) *Nat Biotechnol* 23:709–717.
4. Zimmermann TS, Lee ACH, Akinc A, Bramlage B, Bumcrot D, Fedoruk MN, Harborth J, Heyes JA, Jeffs LB, John M, *et al.* (2006) *Nature* 441:111–114.
5. Behlke MA (2006) *Mol Ther* 13:644–670.
6. Bartlett DW, Davis ME (2007) *Bioconjugate Chem* 18:456–468.
7. Kircheis R, Wightman L, Schreiber A, Robitza B, Rossler V, Kursa M, Wagner E (2001) *Gene Ther* 8:28–40.
8. Kircheis R, Ostermann E, Wolschek MF, Lichtenberger C, Magin-Lachmann C, Wightman L, Kursa M, Wagner E (2002) *Cancer Gene Ther* 9:673–680.
9. Park JW, Hong K, Kirpotin DB, Colbern G, Shalaby R, Baselga J, Shao Y, Nielsen UB, Marks JD, Moore D, *et al.* (2002) *Clin Cancer Res* 8:1172–1181.
10. Hu-Lieskovan S, Heidel JD, Bartlett DW, Davis ME, Triche TJ (2005) *Cancer Res* 65:8984–8992.
11. Pun SH, Bellocq NC, Cheng J, Grubbs BH, Jensen GS, Davis ME, Tack F, Brewster M, Janicot M, Janssens B, *et al.* (2004) *Cancer Biol Ther* 3:31–40.
12. Kirpotin DB, Drummond DC, Shao Y, Shalaby MR, Hong K, Nielsen UB, Marks JD, Benz CC, Park JW (2006) *Cancer Res* 66:6732–6740.
13. Wu AM, Yazaki PJ, Tsai S-W, Nguyen K, Anderson A-L, McCarthy DW, Welch MJ, Shively JE, Williams LE, Raubitschek AA, *et al.* (2000) *Proc Natl Acad Sci USA* 97:8495–8500.
14. Medarova Z, Pham W, Farrar C, Petkova V, Moore A (2007) *Nat Med* 13:372–377.
15. Bartlett DW, Davis ME (2006) *Nucleic Acids Res* 34:322–333.
16. Bartlett DW, Davis ME (2007) *Biotechnol Bioeng* 97:909–921.
17. Loening AM, Gambhir SS (2003) *Mol Imaging* 2:131–137.
18. Owen J, Charles A, Orvis AL (1970) *Am J Physiol* 218:88–91.
19. van de Water FM, Boerman OC, Wouterse AC, Peters JGP, Russel FGM, Masereeuw R (2006) *Drug Metab Dispos* 34:1393–1397.
20. Braasch DA, Paroo Z, Constantinescu A, Ren G, Oz OK, Mason RP, Corey DR (2004) *Bioorgan Med Chem* 14:1139–1143.
21. Liu N, Ding H, Vanderheyden J-L, Zhu Z, Zhang Y (2007) *Nucl Med Biol* 34:399–404.
22. Ogris M, Brunner S, Schuller S, Kircheis R, Wagner E (1999) *Gene Ther* 6:595–605.
23. de Wolf HK, Snel CJ, Verbaan FJ, Schiffelers RM, Hennink WE, Storm G (2007) *Int J Pharm* 331:167–175.
24. Adams GP, Schier R, Marshall K, Wolf EJ, McCall AM, Marks JD, Weiner LM (1998) *Cancer Res* 58:485–490.
25. Maeda N, Miyazawa S, Shimizu K, Asai T, Yonezawa S, Kitazawa S, Namba Y, Tsukada H, Oku N (2006) *Biol Pharm Bull* 29:1936–1940.
26. Chow PL, Stout DB, Komisopoulou E, Chatziioannou AF (2006) *Phys Med Biol* 51:379–390.
27. Yazdi PT, Wenning LA, Murphy RM (1995) *Cancer Res* 55:3763–3771.
28. Riches AC, Sharp JG, Thomas B, Smith SV (1973) *J Physiol* 228:279–284.
29. Kuszyk BS, Corl FM, Franano FN, Bluemke DA, Hofmann LV, Fortman BJ, Fishman EK (2001) *Am J Roentgenol* 177:747–753.